Volume 25
Number 10
14 March 2023
Pages 7051–7552

PCCP

Physical Chemistry Chemical Physics

rsc.li/pccp

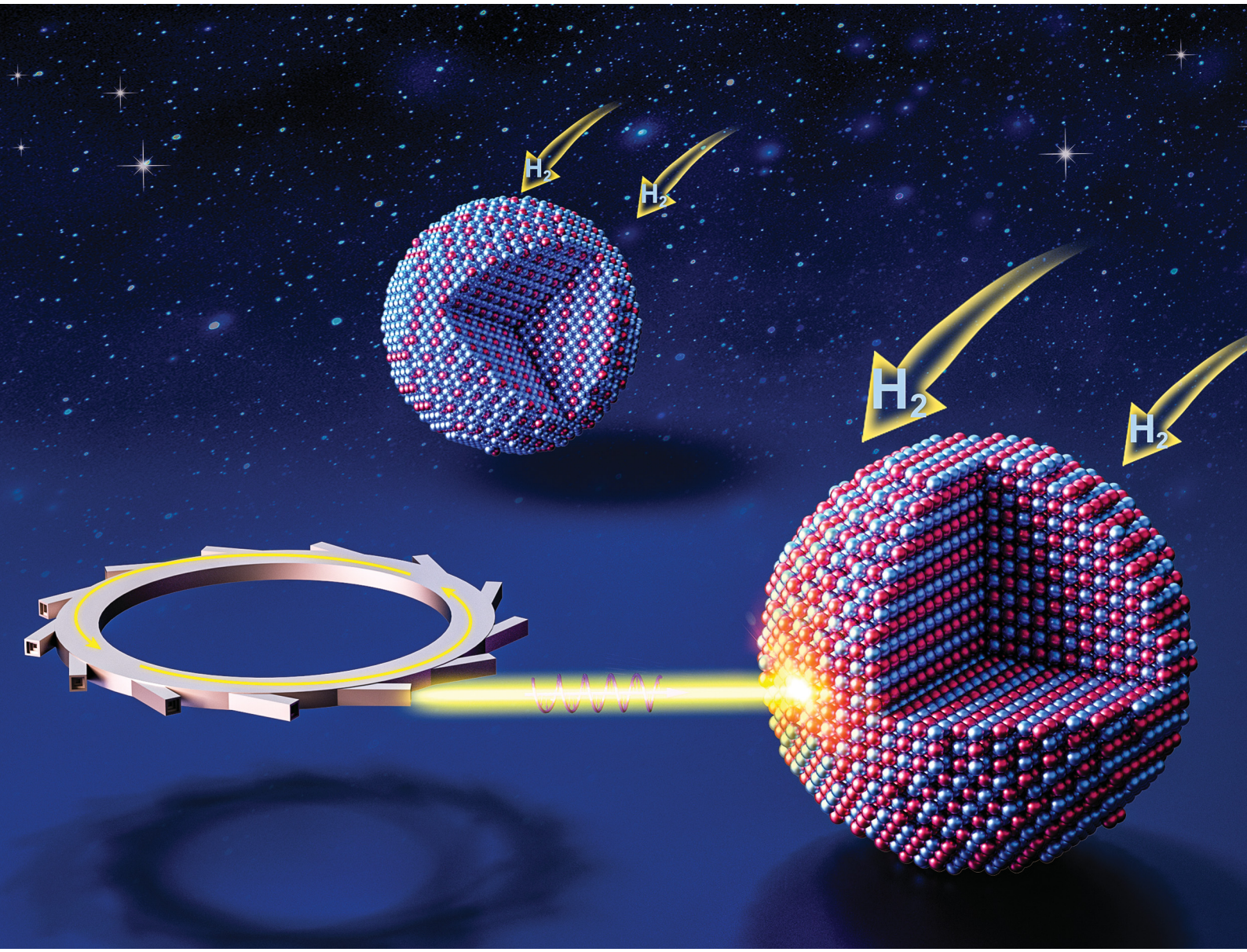

ISSN 1463-9076

ROYAL SOCIETY OF CHEMISTRY

PAPER

Yu Lei *et al.*

Synthesis of Pt_3Zn_1 and Pt_1Zn_1 intermetallic nanocatalysts for dehydrogenation of ethane

PCCP

ROYAL SOCIETY OF CHEMISTRY

PAPER

View Article Online
View Journal | View Issue

Cite this: *Phys. Chem. Chem. Phys.*, 2023, **25**, 7144

Synthesis of Pt_3Zn_1 and Pt_1Zn_1 intermetallic nanocatalysts for dehydrogenation of ethane†

Zhuoran Gan,[a] Zheng Lu,[b] Muntaseer Bunian,[a] Larissa B. Lagria,[a] Christopher L. Marshall,[b] R. Michael Banish,[a] Sungsik Lee[c] and Yu Lei *[a]

Received 7th September 2022,
Accepted 31st January 2023

DOI: 10.1039/d2cp04173a

rsc.li/pccp

Pt_3Zn_1 and Pt_1Zn_1 intermetallic nanoparticles supported on SiO_2 were synthesized by combining atomic layer deposition (ALD) of ZnO, incipient wetness impregnation (IWI) of Pt, and appropriate hydrogen reduction. The formation of Pt_1Zn_1 and Pt_3Zn_1 intermetallic nanoparticles was observed by both X-ray diffraction (XRD) and synchrotron X-ray absorption spectroscopy (XAS). STEM images showed that the 2–3 nm Pt-based intermetallic nanoparticles were uniformly dispersed on a SiO_2 support. The relationships between Pt–Zn intermetallic phases and synthesis conditions were established. *In situ* XAS measurements at Pt L_3 and Zn K edges during hydrogen reduction provided a detailed image of surface species evolution. Owing to a combined electronic and geometric effect, Pt_1Zn_1 exhibited much higher reactivity and stability than Pt_3Zn_1 and Pt in both the direct dehydrogenation and oxidative dehydrogenation of ethane to ethylene reactions.

1. Introduction

Single-atom alloys (SAA) are a form of single-atom catalysts that consist of atomically dispersed active sites in a host metal.[1] When the metal active sites and the host metal form a random alloy (*i.e.*, solid solution), atomic dispersion can be achieved by maintaining a low density of active sites.[2] High-density, monodispersed active sites can be achieved if the binary system forms an intermetallic phase.[3] Intermetallic alloys are a type of bimetallic compound that forms a finite stoichiometry and ordered atomic structure which warrants uniform catalytic active sites. Although intermetallic catalysts exhibit greater active site density than the solid solution, the thermodynamically favored intermetallic phases could theoretically resist segregation under heat and chemical adsorption.[4] These features make intermetallic catalysts attractive for applications in well-defined catalysis systems. A Pt–Sn intermetallic alloy is the most studied alloy system in the dehydrogenation of alkanes and has been commercialized.[5] Adding a second metal to Pt can reduce the particle size thus effectively suppressing side reactions, for example, hydrogenolysis and coking.[6] Various new Pt-based intermetallic nanocatalysts, such as Pt–Zn, Pt–In, and Pt–V, have demonstrated enhanced activity and selectivity in alkane dehydrogenation.[7] However, the intrinsic contributions of these add-metals to Pt are still in question, due to the difficulties in the preparation of Pt-based intermetallic nanoparticles with a targeted crystal structure.[8]

Pt–Zn intermetallic nanoparticles have exhibited excellent catalytic performance in electrooxidation,[9] hydrogenation,[10] and dehydrogenation.[11] Catalytic dehydrogenation of light alkanes, such as ethane and propane, is an on-purpose production method that exclusively yields the desired alkene of polymer-quality purity rather than a mixture of products.[12] Cybulskis and coworkers have shown that the intermetallic Pt_1Zn_1 nanoparticles are more active, selective, and stable than the un-promoted Pt nanoparticles in the dehydrogenation of ethane.[7a] They ascribed the improved performance to both electronic and geometric effects. Nevertheless, how exactly these two factors affect the ethane dehydrogenation activity, selectivity, and stability were not well established with the limited examples of Pt_1Zn_1 and metallic Pt. Also, as their work and many recent studies on alkane dehydrogenation using PtZn nanocatalysts[11,13] focused on more characterization on the Pt side, the information on the changes of Zn species was lacking, this might overlook some important aspects for the successful synthesis of active phases. The Pt_1Zn_1 catalyst they prepared utilized incipient wetness impregnation, a relatively rapid method widely used in catalyst synthesis. However, this method is known to produce nanoparticles with broad size distribution. A controlled synthesis method may offer a well-defined catalyst system to establish precise structure and performance relationships.

[a] *Department of Chemical and Materials Engineering, University of Alabama in Huntsville, Huntsville, AL, 35899, USA. E-mail: yu.lei@uah.edu; Tel: +1-256-824-6527*
[b] *Chemical Sciences and Engineering Division, Argonne National Laboratory, Lemont, IL 60439, USA*
[c] *X-ray Science Division, Advanced Photon Source, Argonne National Laboratory, Lemont, IL 60439, USA*

† Electronic supplementary information (ESI) available: XRD patterns, EDX spectrum, EXAFS fitting, and N2 absorption–desorption isotherms. See DOI: https://doi.org/10.1039/d2cp04173a

Chemical methods used to synthesize intermetallic alloy nanoparticles include impregnation, colloidal synthesis, and chemical vapor deposition. Atomic layer deposition (ALD) has emerged as an important technique for thin film deposition.[14] It produces conformal coatings of materials *via* self-limiting chemical reactions between the precursors. By controlling ALD parameters such as dose time, the number of cycles, and deposition temperature, we can quantitatively design catalysts with the desired thickness, loading, and microstructures. ZnO ALD, as one of the well-developed ALD processes,[15] can potentially aid in the design of mono-dispersed nanoscale Pt–Zn intermetallic alloys, such as Pt_3Zn_1, Pt_1Zn_1, Pt_3Zn_{10}, Pt_1Zn_8, *etc.*,[16] which will provide more information regarding Pt site isolation and electronic states with the addition of Zn.

Herein, we synthesized silica-supported Pt_3Zn_1 and Pt_1Zn_1 intermetallic nanocatalysts by sequential deposition of ZnO *via* atomic layer deposition (ALD) and Pt *via* incipient wetness impregnation (IWI) on SiO_2 with H_2 reduction. The synthesis method was examined using standard characterization techniques as well as synchrotron X-ray absorption spectroscopy (XAS) under hydrogen reduction conditions. We revealed that ZnO reduction is a key step in the synthesis of the Pt_1Zn_1 phase by providing a detailed picture of Pt and Zn speciation kinetics under H_2 reduction *via in situ* XAS. Silica-supported Pt_3Zn_1, Pt_1Zn_1, and Pt monometallic nanocatalysts were tested in both dehydrogenation of ethane (DHE) and oxidative dehydrogenation of ethane (ODHE), and the electronic and geometric effects on the catalytic performance of PtZn intermetallic nanocatalysts are discussed thoroughly. The Pt_1Zn_1 intermetallic nanocatalysts exhibited improved selectivity and a production rate one order of magnitude greater than those of supported Pt and Pt_3Zn_1 with similar Pt loading and particle sizes for the dehydrogenation of ethane. Enhanced catalyst stability was also observed.

2. Experimental section

2.1 Synthesis

Synthesis of ZnO/SiO_2. SiO_2 (Silicycle S10040M, 100 m^2 g^{-1}) was used as the catalyst support. ZnO ALD was carried out in a viscous flow benchtop reactor (Gemstar-6, Arradiance) at deposition temperatures of 150 °C and 200 °C. One gram of SiO_2 was spread out smoothly onto a metal tray and covered by a stainless steel wire cloth to prevent powder from spilling out while maintaining sufficient diffusion of the reactants. ZnO ALD was performed using alternating exposure to diethyl zinc (DEZ, Sigma Aldrich) and deionized water. Both DEZ and H_2O were kept in sealed stainless steel bottles at room temperature. One ALD cycle time sequence began with DEZ exposure time (t_1) followed by a N_2 purge time (t_2), then H_2O exposure time (t_3) followed by a second N_2 purge time (t_4).

Synthesis of Pt/SiO_2. Pt was deposited on SiO_2 (pore volume of 0.9 mL g^{-1}) by pH-modified incipient wetness impregnation (IWI). First, 0.4 g of $(NH_3)_4Pt(NO_3)_2$ (Alfa Aesar) was dissolved in 3.42 mL of deionized water. NH_4OH (Fisher Scientific) was subsequently added to the solution to adjust the pH to 11. The solution was then added dropwise to 3.8 g of SiO_2 with constant stirring. The resulting powder was dried at 125 °C in an oven overnight, and then calcined at 300 °C in a tubular furnace for 3 h.

Synthesis of Pt/ZnO/SiO_2. Pt was deposited on ZnO/SiO_2 by impregnation of $(NH_3)_4Pt(NO_3)_2$ solution (pH adjusted to 11). The resulting powder was calcined at 300 °C in a tubular furnace for 3 h.

Synthesis of intermetallic PtZn/SiO_2. The pre-catalyst Pt/ZnO/SiO_2 was reduced in 5% H_2 with balance He (nexAir) at various temperatures between 400 °C and 800 °C to achieve different phases of PtZn intermetallic alloy nanoparticles. The H_2 flow was further treated using a Supelco gas purifier (Sigma Aldrich). In a typical experiment, the sample was heated from room temperature to the targeted temperature using a temperature ramping rate of 2.5 °C min^{-1}; the target temperature was held for a certain period of time before the sample was cooled to room temperature. The Pt_1Zn_1 and Pt_3Zn_1 phases were achieved by hydrogen reduction at 600 °C for 15 min and at 800 °C for 8 h, respectively. The actual loadings of Pt and Zn were determined by ICP-OES.

2.2 Characterization

The thickness of the ZnO film deposited onto the Si(100) wafer was determined by spectroscopic ellipsometry (SE) using a J. A. Woollam alpha-SE variable angle spectroscopic ellipsometer. X-ray Diffraction (XRD) was performed on a Rigaku MiniFlex 600 powder X-ray diffractometer operated at 40 kV and 15 mA. XRD patterns were scanned from $2\theta = 10°$ to 90° with a scanning speed of 1° min^{-1}. Brunauer–Emmett–Teller (BET) surface area measurements were performed using a gas sorption analyzer (Autosorb iQ, Quantachrome Instruments) at 77 K. In a typical experiment, the sample was outgassed at 350 °C for 10 h. The specific surface area was calculated using the Brunauer–Emmett–Teller (BET) method and the pore volume and size were obtained using the Barrett–Joyner–Halenda (BJH) method. Pt dispersions based on H_2 chemisorption were also estimated using the Autosorp iQ gas sorption analyzer. All samples were heated *in situ* to 600 °C, held for 2 h under H_2 (Airgas, 99.999%), and evacuated for 2 h before cooling to 40 °C for chemisorption. The STEM images were taken at the Center for Nanoscale Materials within the Argonne National Laboratory using a FEI Talos scanning transmission electron microscope. A TEM grid was first mixed with the sample inside a vial by shaking rigorously. Images were then taken using a high-angle annular dark-field (HAADF) detector at 300 kV. The energy-dispersive X-ray (EDX) spectra of the catalysts were taken using a JEOL 2100 TEM equipped with a Gatan camera at an accelerating voltage of 200 kV. Inductively coupled plasma optical emission spectroscopy (ICP-OES) was carried out using an Agilent 5110 SVDV ICP-OES spectrometer.

X-ray absorption spectroscopy (XAS) measurements were conducted at 12-BM of the Advanced Photon Source (APS) at the Argonne National Laboratory. Transmission mode spectra were taken at the Pt L_3 edge (~11 564 eV) and the Zn K edge

(~9659 eV). For the *ex situ* measurements, Pt/SiO_2, Pt_1Zn_1/SiO_2, and Pt_3Zn_1/SiO_2 samples were first reduced in 3.5% H_2 with balance He at 600 °C for 30 min to remove any surface oxides which formed due to sample transfer. The samples were then cooled and measured in helium at RT. For the *in situ* XAS study, the $Pt/ZnO/SiO_2$ precatalyst was reduced by 3.5% H_2/He at the designated temperature for 15 min and then measured at RT under helium protection. The XANES linear combination fittings were processed from Athena in the normalized $\mu(E)$ space, with Pt metal foil and PtO_2 used as references. The fittings were done in the range of 10 eV below and 40 eV above the Pt L_3 edge. EXAFS regime data fittings were performed using Artemis in the IFEFFIT software package.

2.3 Catalytic performance

Direct dehydrogenation of ethane (DHE) and oxidative dehydrogenation of ethane (ODHE) were carried out in a quartz tube reactor (10 mm I.D.) at 550 °C under atmospheric pressure. The quartz tube was placed in an electric furnace and sealed with Ultra Torr fittings. A K-type thermocouple was used to measure the temperature of the catalyst bed. The catalyst particles sieved between 180 to 250 μm were mixed with 500 mg 60/80 mesh quartz chips. For DHE, the catalyst weight is fixed at 100 mg to achieve a weight hourly space velocity (WHSV) of 7.2 h^{-1}. The reactant feed used in DHE was composed of 18% C_2H_6 (Matheson, 99.99%) and 82% He (nexAir, 99.999%), for a total flow of 50 mL min^{-1}. For ODHE, the reactant feed contained 22.3% ethane and 1.7% oxygen with balance helium. Due to the rapid deactivation in ODHE, various amounts of catalysts were used to achieve ~10% initial conversion. The amount used for Pt, Pt_1Zn_1, and Pt_3Zn_1 were 250 mg, 10 mg, and 90 mg, respectively. The effluent line was heated to temperatures above 80 °C to prevent condensation of byproducts. Before each reaction, the catalyst was reduced by 5% H_2/He at 600 °C for 30 min. The effluents were analyzed on a gas chromatograph (SRI, 310C) equipped with a ShinCarbon ST column and a thermal conductivity detector (TCD).

3. Results and discussion

Uniform ZnO thin films formed on SiO_2 support *via* atomic layer deposition acted as the source of Zn for the preparation of nano-sized Pt–Zn intermetallic alloys. As shown in Fig. 1(a), the linear growth behavior of ZnO thin films yielded a growth per cycle (GPC) of ~1.8 Å per cycle. This growth rate is consistent with the 1.5–1.9 Å per cycle range within the 50–300 °C temperature range found in the literature.[17] The saturation exposure of DEZ for deposition of ZnO on high surface area SiO_2 powder was determined by varying the DEZ exposure time from 0.5 to 10 s, as shown in Fig. 1(b). The saturation weight gain was ~7 wt% when the dose time of DEZ reached 5 s (~6.7 wt% at 150 °C, ~7.0 wt% at 200 °C). The formation of metallic Zn within the thin films was observed at 200 °C (Fig. 1(c)). This incorporation of metallic Zn was likely due to the thermal decomposition of DEZ on the substrate,[18] but the saturation weight gain suggests that the nature of the ZnO growth was within the ALD regime.[19] Based on the surface area of SiO_2 and the density of ZnO, the theoretical saturated weight gain is calculated to be ~9.7 wt%. The weight gain is lower than expected, which indicates that ZnO ALD precursors cannot access the entire surface of SiO_2 due to steric hindrance.[15] The time sequence of 5-200–37.5-200 s and deposition temperature of 200 °C were used to prepare ZnO/SiO_2. Pt nanoparticles were subsequently deposited on the ZnO-covered SiO_2 surface *via* incipient wetness impregnation (IWI).

The Pt–Zn intermetallic phases were generated by reducing $Pt/ZnO/SiO_2$ in hydrogen. The optimal reduction temperature was determined by varying the temperature between 600 °C and 800 °C, while the optimal reduction time was determined by varying the length of time at which $Pt/ZnO/SiO_2$ was reduced,

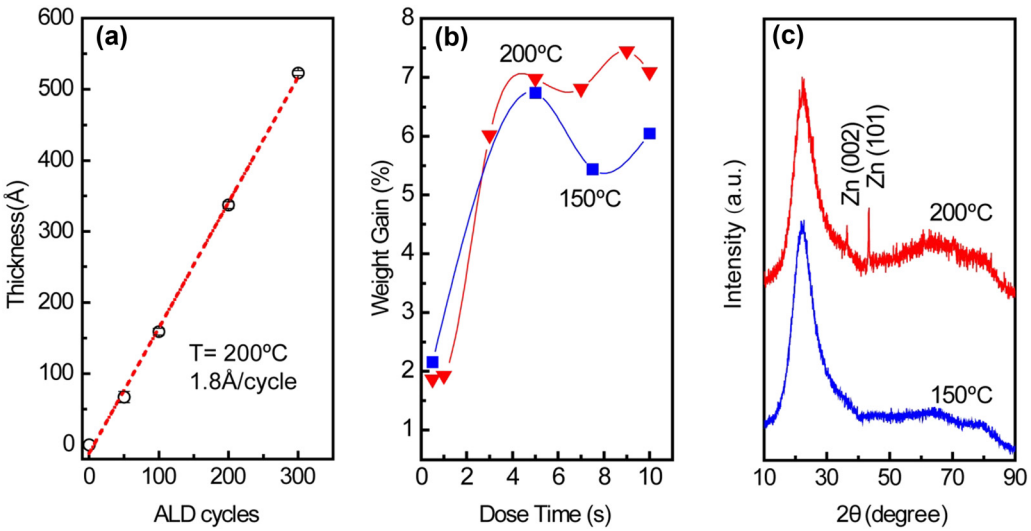

Fig. 1 (a) Growth rate of ZnO ALD at 200 °C with time sequence 0.03-10–0.1-10 s, (b) weight gain as a function of DEZ dose time with time sequence t_1-200–40-200 s, (c) XRD of the ALD ZnO/SiO_2 sample prepared at 150 °C and 200 °C.

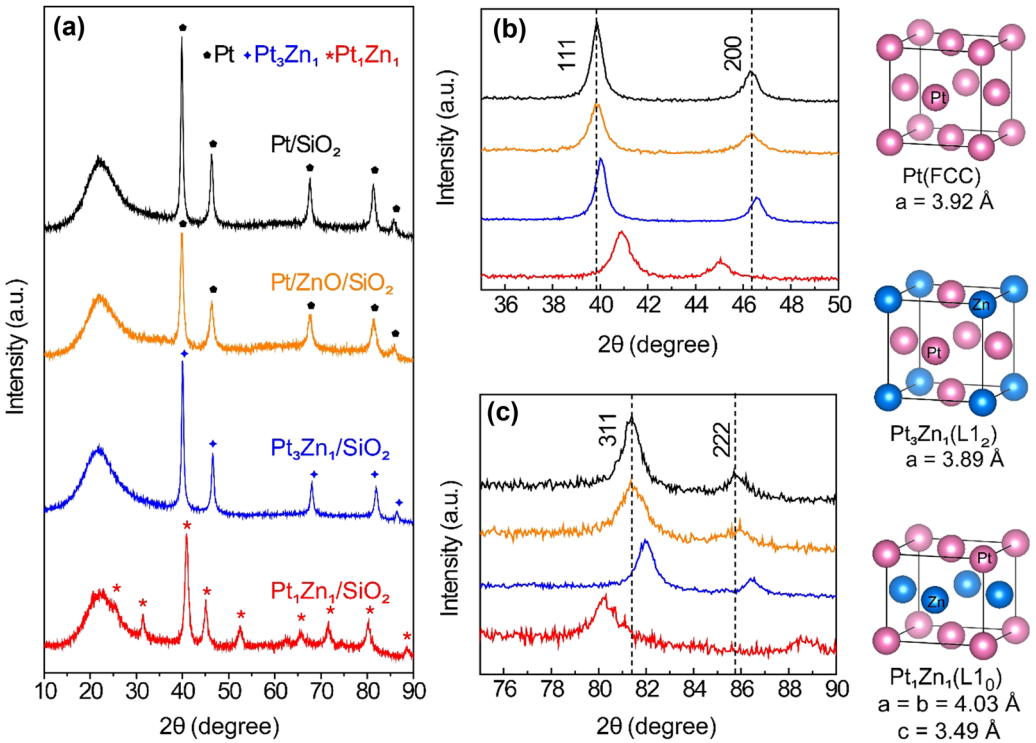

Fig. 2 (a) XRD patterns of Pt/SiO_2, pre-catalyst $Pt/ZnO/SiO_2$, Pt_3Zn_1/SiO_2 and Pt_1Zn_1/SiO_2. Detailed scans of XRD patterns of the four samples between (b) 35–50° and (c) 75–90°.

from 15 min to 10 h, as shown in Fig. S1 (ESI†). The best preparation conditions to generate Pt_1Zn_1 and Pt_3Zn_1 phases were determined to be 6 h reduction at 600 °C and 8 h reduction at 800 °C, respectively. The stoichiometry of the as-prepared Pt_1Zn_1 and Pt_3Zn_1 intermetallics were confirmed using EDX (Fig. S2, ESI†) and ICP-OES. Fig. 2(a) shows that the shape of the XRD pattern of Pt_3Zn_1 (JCPDS no. 65-3257) resembles that of the monometallic Pt phase (JCPDS no. 65-2868) but the peaks are positioned at higher diffraction angles, as shown in the detailed scans in Fig. 2(b) and (c). The shifts in peak location in the Pt_3Zn_1 XRD pattern are evidence that Zn has been incorporated into Pt's face-centered cubic (FCC) structure since Zn has a smaller atomic radius.[20] Based on the XRD patterns, the lattice parameters are calculated to be 3.92 Å for FCC Pt and 3.89 Å for the $L1_2$ Pt_3Zn_1, respectively, and 4.03 Å and 3.49 Å for the *a* and *c* unit vectors, respectively, of the AuCu $L1_0$ tetragonal structured Pt_1Zn_1 (JCPDS no. 06-0604). The Pt–Pt bond distance for Pt/SiO_2, Pt_3Zn_1/SiO_2, and Pt_1Zn_1/SiO_2 nanoparticles are calculated to be 2.77 Å, 2.75 Å, and 2.85 Å (Table S1, ESI†), respectively, which are similar to literature values.[7a,9c,21]

The formation of Pt–Zn intermetallic alloys was further investigated using XAS measurements at Pt L_3 (11.564 keV) and Zn K (9.659 keV) edges. Prior to carrying out XAS measurements, the Pt-containing samples were reduced by 3.5% hydrogen at 600 °C for 30 min to remove any surface oxides that formed due to sample transfer. As compared with the Pt L_3 XANES spectrum of Pt/SiO_2, the whiteline intensities ($2p \rightarrow 5d$ transition) of Pt_3Zn_1/SiO_2 and Pt_1Zn_1/SiO_2 remain nearly the same but their edge positions shift to higher photon energies by 1.5 and 2.4 eV, respectively. These positive shifts indicate changes in hybridization and lower 5d electronic density (Fig. 3(a)).[7a,21,22] At the Zn K-edge, whitelines of Pt_3Zn_1/SiO_2 and Pt_1Zn_1/SiO_2 do not show obvious shifts as compared with metallic Zn, but their intensities are higher (Fig. 3(c)). This feature, corresponding to the $1s \rightarrow 4p$ transition, is sensitive to the change of coordination of Zn and bond distance due to the formation of the Pt–Zn intermetallic phase.[23]

The Pt L_3 edge EXAFS spectrum of $Pt/ZnO/SiO_2$ in Fig. 3(b) shows a Pt–O peak at ~ 1.7 Å and three peaks between 2 Å and 3 Å, indicating the Pt was partially oxidized. The EXAFS spectrum of Pt_1Zn_1 shows a Pt–Zn single peak at ~2.4 Å (uncorrected) while the Pt_3Zn_1 spectrum contains a cluster of three peaks between 2 Å and 3 Å resembling that of Pt owing to their similar crystalline structure. Data fitting in Table S2 and Fig. S3 (ESI†) shows that each Pt atom on Pt/SiO_2 has an average of 10.5 nearest neighbors at a bond distance of 2.76 Å. With the incorporation of Zn, the number of nearest Pt neighbors surrounding one Pt atom in Pt_3Zn_1/SiO_2 decreases to 6.1 and the Pt–Pt bond distance is shortened to 2.73 Å. In Pt_1Zn_1 nanoparticles, the Pt–Pt bond distance is elongated to 2.85 Å and each Pt atom has an average of 3.1 nearest Pt neighbors, indicating that these Pt atoms were structurally more isolated. The bond distances determined by EXAFS data fittings are comparable to those obtained from XRD patterns. In the Zn K edge EXAFS spectra (Fig. 3(d)) and data fitting (Table S3 and Fig. S4, ESI†), ZnO and Zn have single peaks at ~1.5 Å (Zn–O) and 2.3 Å (Zn–Zn), respectively. In the bulk structure of metallic

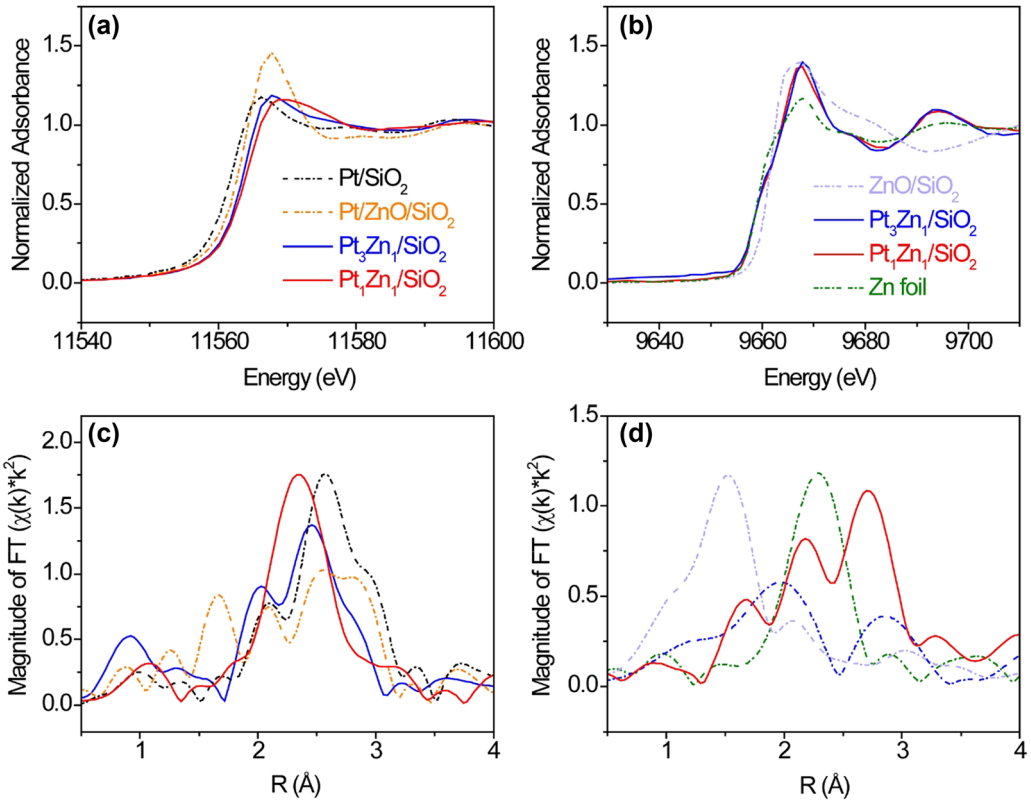

Fig. 3 Pt L_3 edge (a) XANES and (b) EXAFS Fourier transform of Pt/SiO_2, $Pt/ZnO/SiO_2$, Pt_1Zn_1/SiO_2, Pt_3Zn_1/SiO_2. Zn K edge (c) XANES and (d) EXAFS Fourier transform of Zn, ZnO/SiO_2, Pt_1Zn_1/SiO_2, and Pt_3Zn_1/SiO_2.

Zn, each Zn atom has 6 Zn neighbors, with a bond distance of 2.64 Å between atoms. The Zn–Pt bond distances in Pt_3Zn_1 and Pt_1Zn_1 are 2.73 Å and 2.65 Å, respectively, consistent with the bond distances derived from Pt L_3 EXAFS data fitting (Table S2, ESI†) and XRD patterns (Table S1, ESI†).

Fig. 4 shows the STEM images and particle size distribution histograms of Pt/SiO_2, Pt_3Zn_1/SiO_2, and Pt_1Zn_1/SiO_2. The nanoparticles were well dispersed on the SiO_2 support. The particle size distribution, calculated for more than 500 nanoparticles, demonstrates that the average diameter of Pt/SiO_2, Pt_1Zn_1/SiO_2, and Pt_3Zn_1/SiO_2 nanoparticles are all about 2.2 nm. In the EDX mapping, all Pt and Zn co-locate at the same spots, suggesting a homogeneous formation of Pt–Zn alloys.

In situ XAS spectra at Pt L_3 and Zn K edge were measured during hydrogen reduction to determine the surface species evolution. The measurements were obtained by quickly switching between Pt L_3 and Zn K edges (<1 min), and thus the data on both edges were taken almost simultaneously. Fig. 5 shows the XANES and EXAFS spectra at Pt L_3 and Zn K edges during reduction of $Pt/ZnO/SiO_2$ from 25 °C to 800 °C. The *in situ* XAS spectra clearly show the transition from the initial oxidation state to the final intermetallic phase. In Fig. 5(a) and (b), the Pt L_3 edge whiteline gradually shifts to a higher energy, accompanied by the shift of Zn K edge to a lower energy. In the EXAFS spectra in Fig. 5(c) and (d), Pt–Zn bonds arise with the elimination of Pt–O and Zn–O bonds. The quantitative changes to an atom's nearest neighbors and the associated bond distance with respect to Pt and Zn are summarized in Tables S4 and S5 (ESI†), and the fitting quality is shown in Fig. S5–S8 (ESI†).

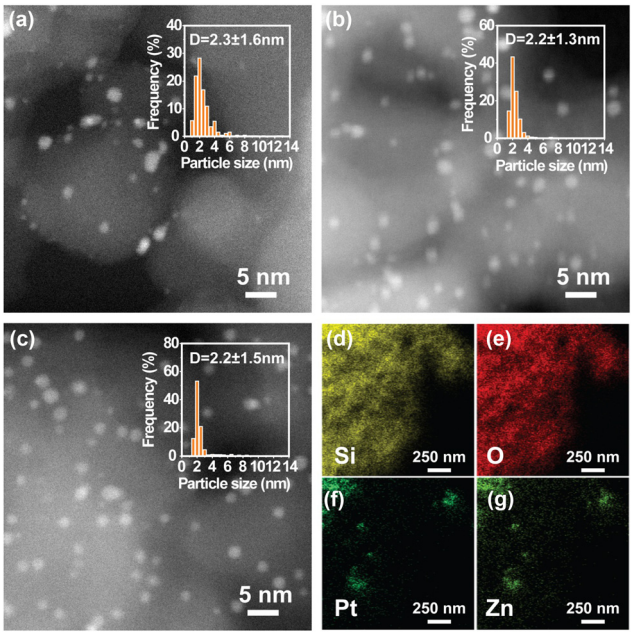

Fig. 4 (a) and (b) HAADF-STEM images and particle size distribution histograms of (a) Pt/SiO_2, (b) Pt_3Zn_1/SiO_2, (c) Pt_1Zn_1/SiO_2, and (d)–(g) EDX mapping of Pt_1Zn_1/SiO_2.

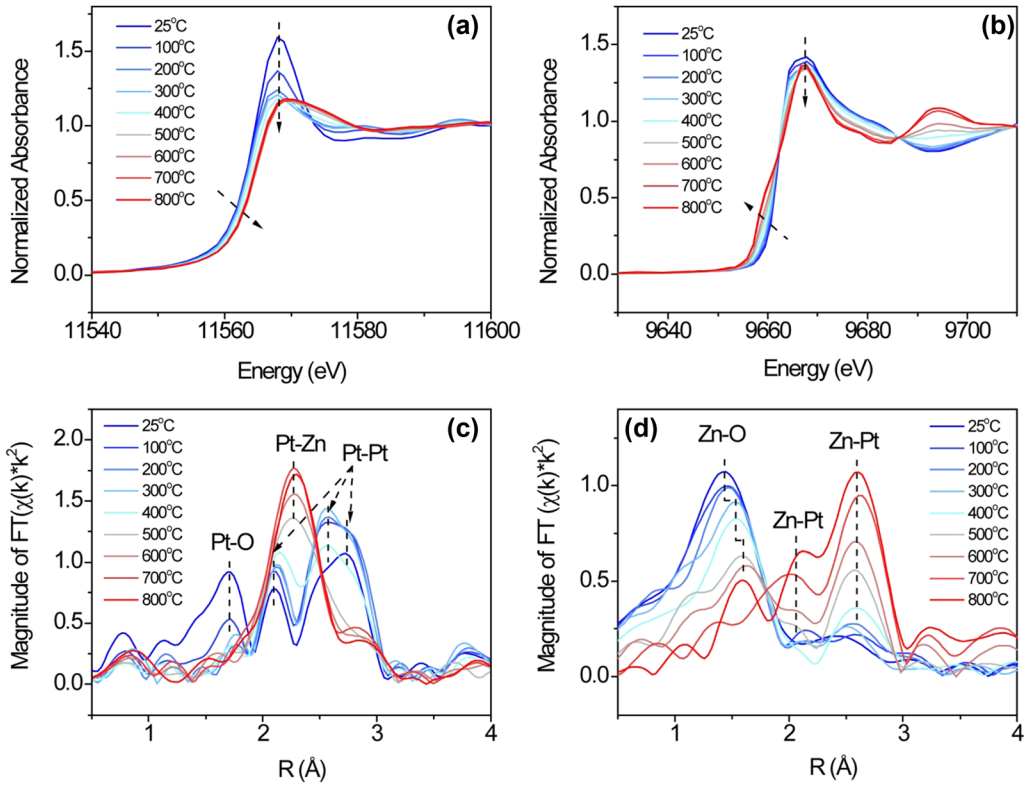

Fig. 5 Pt L_3 edge (a) XANES, (b) EXAFS Fourier transform of Pt/ZnO/SiO_2 during *in situ* hydrogen reduction at elevated temperatures and their Zn K edge XANES (e) and (d) EXAFS counterparts.

XANES linear combination fittings (LCF, Fig. 6) are consistent with the EXAFS fittings summarized in Tables S4 and S5 (ESI†). The as-prepared Pt/ZnO/SiO_2 sample was initially partially oxidized, containing 69% metallic Pt and 31% PtO_2, while all the zinc was in the form of ZnO. PtO_2 was completely reduced to the metallic state at 200 °C, coinciding with the formation of the Pt–Zn phase and conforming to previous studies on hydrogen reduction of Pt/ZnO/Al_2O_3 and Pd/ZnO.[24]

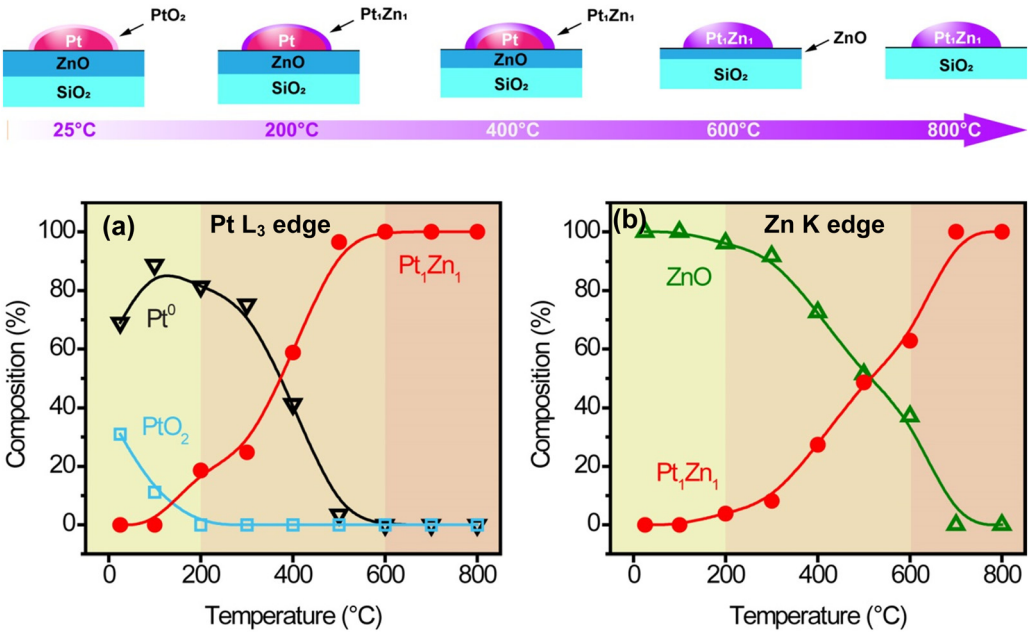

Fig. 6 (a) Scheme of surface species evolution, and XANES linear combination fitting (LCF) of (b) Pt L_3 and (c) Zn K edges.

The hydrogen reduction was likely catalyzed by platinum, which was able to reduce Zn at such a low temperature. Upon increasing temperature from 200 °C to 600 °C, more Pt–Zn phase formed as more ZnO was reduced. The formation of Pt_1Zn_1 seems to be limited by the catalytic reduction rate of ZnO instead of Zn atom diffusion into Pt. At 600 °C, all platinum existed in the form of Pt_1Zn_1 phase while excess ZnO remained. The excess ZnO could be removed by long reduction or vaporization at higher temperature, *i.e.*, 800 °C. Note that it was still in the Pt_1Zn_1 phase as it took 8 hours at 800 °C to form the Pt_3Zn_1 phase (Fig. S1b, ESI†).

There are three main concerns regarding the reduction of the $Pt/ZnO/SiO_2$ sample to Pt_3Zn_1/SiO_2 at 800 °C in hydrogen. The first concern is the possible collapse of the porous SiO_2 support, which will cause a close encapsulation of platinum and prevent reactants from accessing the catalyst's active sites. The second concern is the occurrence of sintering of platinum nanoparticles due to diffusion-coalescence at high temperatures and a hydrogen environment, again leading to the loss of active sites for catalytic reactions. The last concern is the potential formation of the Pt–Si phase induced by platinum-catalyzed SiO_2 reduction. The latter two concerns were observed in an *in situ* TEM study of Pt/SiO_2 reduction at 800 °C in hydrogen.[25] The diameter of Pt nanoparticles increased from 2 nm to 4.8 nm, which is associated with the formation of Pt_3Si after being reduced in hydrogen at 800 °C. In our study, these three concerns were ruled out as evidenced by combining BET surface area analysis, XRD patterns, and EXAFS spectra. As shown in Fig. S9 and Table S6 (ESI†), the surface area, pore diameter, and pore volume are consistent between $Pt/ZnO/SiO_2$, Pt_1Zn_1/SiO_2, and Pt_3Zn_1/SiO_2, indicating that the structural integrity of SiO_2 support was maintained. Neither any Pt–Si phase was observed in XRD patterns, nor was Pt–Si present in the EXAFS spectra. As the SiO_2 support was uniformly covered by ZnO deposited by ALD, it may have prevented the contact between Pt and SiO_2 and the possible subsequent formation of Pt_3Si.

The dehydrogenation of ethane reaction at 550 °C with a WHSV of 7.2 h^{-1} was used to evaluate the catalytic performance of the Pt–Zn intermetallic nanoparticles. Catalytic performance results are shown in Fig. 7. Based on the Pt dispersion (Table S6, ESI†), the initial ethylene turnover frequency (TOF), normalized per surface Pt was 0.56 s^{-1} for Pt_1Zn_1/SiO_2, much higher than the Pt-rich Pt_3Zn_1/SiO_2 (0.48 s^{-1}) and the monometallic Pt/SiO_2 (0.04 s^{-1}). Although all three catalysts had close to 100% C_2H_4 selectivity, the Pt_1Zn_1 catalyst exhibited significantly improved stability. The Pt_1Zn_1 catalyst maintained at a higher conversion (~24.5%) during the reaction period as compared to the Pt_3Zn_1 whose conversion rapidly decreased from 7% to 1.7%.

As shown in Fig. 8, the Pt_1Zn_1 catalysts also exhibited the best performance in terms of C_2H_4 TOFs, conversion, and selectivity in the ODHE. The time-on-stream catalytic tests demonstrate that Pt/SiO_2 has an initial C_2H_4 TOF of 0.04 s^{-1} and a C_2H_4 selectivity of 70.2%, and the selectivity decays rather quickly during the first hour, with 39.3% left after 5 h. The Pt-rich Pt_3Zn_1/SiO_2 exhibited better initial C_2H_4 TOF (0.66 s^{-1}) and selectivity (77%) as compared to Pt/SiO_2, but after 2 h the selectivity drops steeply and almost follows the decay path of Pt/SiO_2. Pt_1Zn_1/SiO_2 shows not only improved initial C_2H_4 TOF (2.79 s^{-1}, 70 times higher than Pt/SiO_2) and C_2H_4 selectivity (89.4%), but also more stable. Its selectivity did not show a drastic decrease and remained at 67.2% after 5 h. It is shown in Fig. 8d that the main by-products for ODHE are CO, CO_2, and CH_4, the CO plus CO_2 initial selectivity for Pt/SiO_2 is the highest, revealing that Pt monometallic is favorable for the combustion reaction path.

The improved performance may be caused by the combined electronic and geometry effects due to the presence of Zn in Pt.[7a,24a] Cybulskis observed that Pt_1Zn_1/SiO_2 was more active and stable than Pt/SiO_2 in dehydrogenation of ethane. By using density functional theory (DFT) calculations and synchrotron resonant inelastic X-ray spectroscopy (RIXS), they attributed the improvement to the electronic effect where the structure of Pt 5d valence orbitals changed due to the presence of Zn. Our studies by including the performance of an additional Pt_3Zn_1/SiO_2 intermetallic catalysts support their conclusion. The improved performance of Pt_1Zn_1/SiO_2 is more likely due to a combined electronic and geometric effect. In other words, the electronic states of Pt 5d are changed by adding the Zn element. As shown by XANES in Fig. 3(a), the Pt L_3 edge

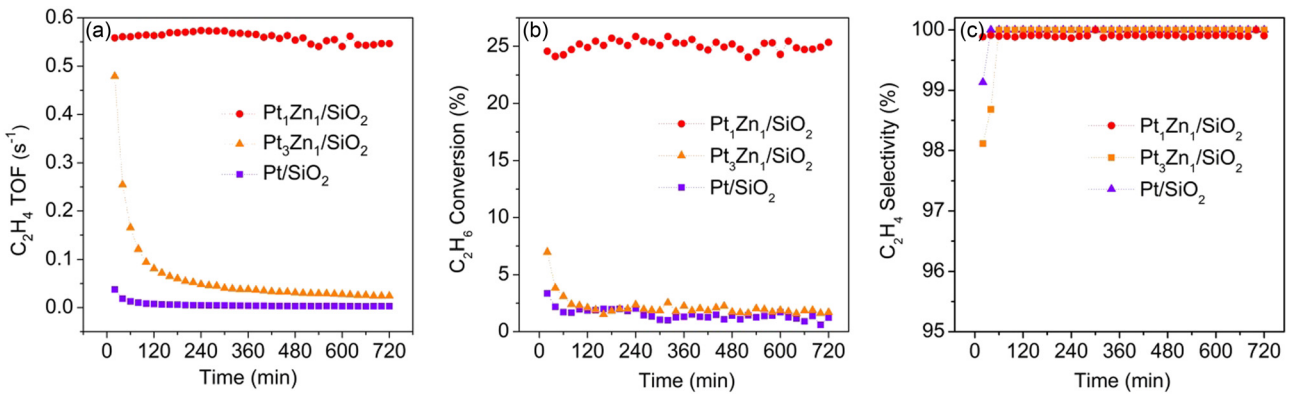

Fig. 7 (a) C_2H_4 TOF s^{-1}, (b) C_2H_6 conversion and (c) C_2H_4 selectivity as a function of reaction time (reaction conditions: T = 550 °C, C_2H_6 = 18% with balance He. 100 mg catalyst was used for each test. All catalysts were pre-treated with 5% H_2/He for 30 min at 600 °C before DHE, WHSV = 7.2 h^{-1}).

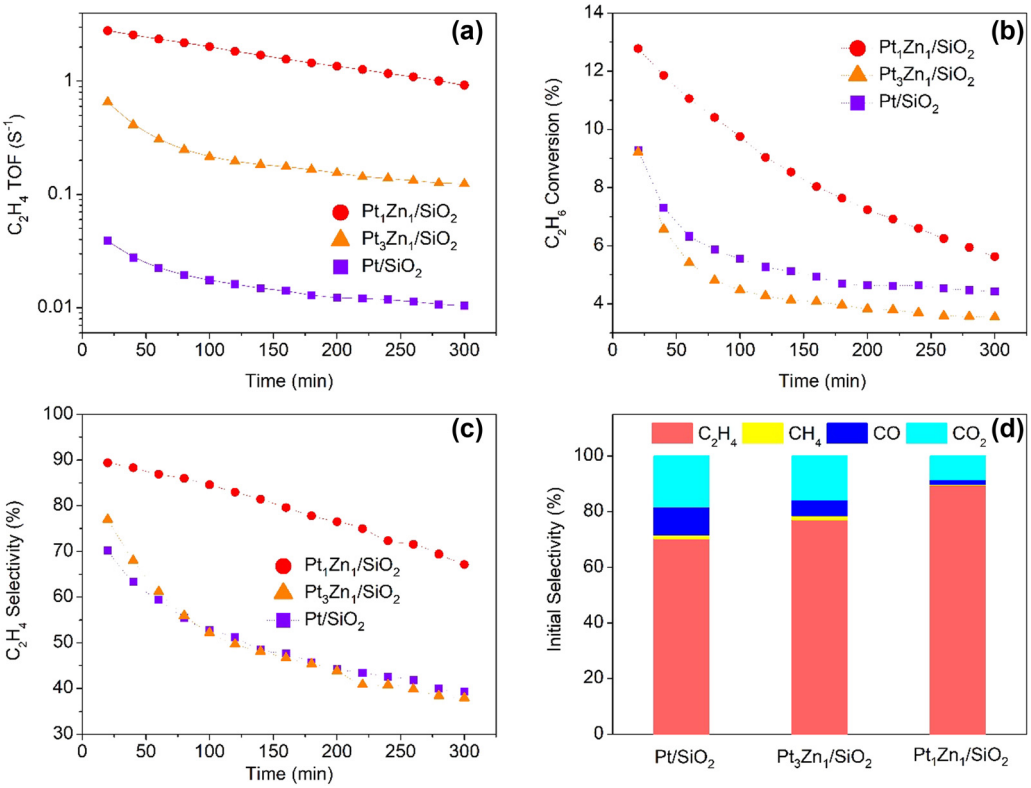

Fig. 8 (a) C_2H_4 TOF, (b) C_2H_6 conversion and (c) C_2H_4 selectivity as a function of reaction time. (d) Initial selectivity of the product gases on the catalysts. (Reaction conditions: T = 550 °C, C_2H_6 = 22.3%, O_2 = 1.7%, He = 76%, total flowrate = 50 ml min^{-1}. All catalysts were pre-treated with 5% H_2/He for 30 min at 600 °C before ODHE, initial conversion was at ~10% for all catalysts).

position of Pt_1Zn_1 and Pt_3Zn_1 shifted to higher energy by 2.4 eV and 1.5 eV, respectively, compared with Pt monometallic. Those shifts in edge energy reflect an upward shift of unfilled Pt 5d bands, which also cause a downward shift of filled 5d bands. These energy changes are related to the bonding of Pt and the adsorbate, which in turn affects the catalytic turnover on the Pt active site. These results are consistent with the initial performance of the catalyst in the order of Pt_1Zn_1 > Pt_3Zn_1 > Pt/SiO_2 in both DHE and ODHE reactions. Regarding the geometric effect, the Pt atoms are atomically more isolated in Pt_1Zn_1 (CN_{Pt-Pt} = 3.1, R_{Pt-Pt} = 2.85 Å) than in either Pt_3Zn_1 (CN_{Pt-Pt} = 6.1, R_{Pt-Pt} = 2.73 Å) or Pt (CN_{Pt-Pt} = 10.5, R_{Pt-Pt} = 2.76 Å). The C_2H_4 TOF for both DHE and ODHE are compared with those state-of-the-art Pt-based catalysts from the literature (Tables S7 and S8, ESI†), Pt_1Zn_1/SiO_2 shows comparable or enhanced C_2H_4 TOF with other Pt–Zn or Pt–Sn nanocatalysts, considering our reaction temperature and space velocity. The more isolated Pt in Pt_1Zn_1 may be responsible for the improved catalyst stability as it slows the coke deposition. The use of intermetallic alloys could be a promising approach to synthesize well-defined, atomically dispersed catalysts.

4. Conclusions

Pt_1Zn_1/SiO_2 and Pt_3Zn_1/SiO_2 intermetallic nanocatalysts were synthesized by sequential deposition of ZnO (by ALD) and Pt (by IWI) on a SiO_2 support, followed by hydrogen reduction with suitable temperature and length of time. In particular, the hydrogen reduction of $Pt/ZnO/SiO_2$ was investigated using *in situ* synchrotron X-ray absorption spectroscopy at both Pt L_3 and Zn K edges. The Pt_1Zn_1 intermetallic phase was formed at temperatures as low as 200 °C by the platinum catalyzed reduction. The formation rate of Pt_1Zn_1 was controlled by the ZnO reduction, not by diffusion of the metallic Zn into Pt. All Pt was completely in the Pt_1Zn_1 phase at 600 °C while excess ZnO still existed on the support. A higher temperature (at 800 °C for 15 min) or longer reduction time (at 600 °C for 6 h) is necessary to remove the excess ZnO and reach the Pt : Zn = 1 : 1 stoichiometry on the surface. Further reduction at 800 °C for 8 h will result in the Pt_3Zn_1 phase.

Pt_1Zn_1/SiO_2 exhibited an ethylene TOF much higher than those of Pt_3Zn_1/SiO_2 and Pt/SiO_2 in direct dehydrogenation and oxidative hydrogenation of ethane to ethylene. The Pt_1Zn_1/SiO_2 catalysts also exhibited considerably enhanced stability. The presence of Zn in Pt–Zn intermetallic alloys leads to both electronic structure and geometric structure changes of Pt. The electronic structure of Pt 5d orbitals, which concerns and influences the nanoparticle's catalytic properties, is similar in both Pt_1Zn_1 and Pt_3Zn_1, as determined by the Pt L_3 XAS spectra. This may explain the initial high TOF of both catalysts as compared to the Pt catalyst. The improved stability of Pt_1Zn_1 is likely associated with the geometric effect, as the Pt atoms in Pt_1Zn_1 are significantly more atomically isolated than the Pt atoms in Pt_3Zn_1 and Pt.

Conflicts of interest

There are no conflicts of interest to declare.

Acknowledgements

This work is sponsored by the American Chemical Society Petroleum Research Fund (56197-DNI5). Z. G. gratefully acknowledges a fellowship from the Alabama EPSCoR Graduate Research Scholars Program. This research used resources of the Advanced Photon Source, a U.S. Department of Energy (DOE) Office of Science User Facility, operated for the DOE Office of Science by Argonne National Laboratory under contract no. DE-AC02-06CH11357.

References

1 G. Giannakakis, M. Flytzani-Stephanopoulos and E. C. H. Sykes, Single-Atom Alloys as a Reductionist Approach to the Rational Design of Heterogeneous Catalysts, *Acc. Chem. Res.*, 2019, **52**(1), 237–247.

2 (*a*) X. Zhang, G. Cui, H. Feng, L. Chen, H. Wang, B. Wang, X. Zhang, L. Zheng, S. Hong and M. Wei, Platinum–copper single atom alloy catalysts with high performance towards glycerol hydrogenolysis, *Nat. Commun.*, 2019, **10**(1), 5812; (*b*) P. Aich, H. Wei, B. Basan, A. J. Kropf, N. M. Schweitzer, C. L. Marshall, J. T. Miller and R. Meyer, Single-Atom Alloy Pd–Ag Catalyst for Selective Hydrogenation of Acrolein, *J. Phys. Chem. C*, 2015, **119**(32), 18140–18148; (*c*) J. Liu, F. R. Lucci, M. Yang, S. Lee, M. D. Marcinkowski, A. J. Therrien, C. T. Williams, E. C. H. Sykes and M. Flytzani-Stephanopoulos, Tackling CO Poisoning with Single-Atom Alloy Catalysts, *J. Am. Chem. Soc.*, 2016, **138**(20), 6396–6399.

3 (*a*) S. Furukawa and T. Komatsu, Intermetallic Compounds: Promising Inorganic Materials for Well-Structured and Electronically Modified Reaction Environments for Efficient Catalysis, *ACS Catal.*, 2017, **7**(1), 735–765; (*b*) A. Dasgupta and R. M. Rioux, Intermetallics in catalysis: An exciting subset of multimetallic catalysts, *Catal. Today*, 2019, **330**, 2–15.

4 (*a*) R. J. Meyer, Q. Zhang, A. Kryczka, C. Gomez and R. Todorovic, Perturbation of Reactivity with Geometry: How Far Can We Go?, *ACS Catal.*, 2018, **8**(1), 566–570; (*b*) K. Kovnir, M. Armbrüster, D. Teschner, T. V. Venkov, F. C. Jentoft, A. Knop-Gericke, Y. Grin and R. Schlögl, A new approach to well-defined, stable and site-isolated catalysts, *Sci. Technol. Adv. Mater.*, 2007, **8**(5), 420–427.

5 (*a*) H. N. Pham, J. J. Sattler, B. M. Weckhuysen and A. K. Datye, Role of Sn in the Regeneration of Pt/gamma-Al(2)O(3) Light Alkane Dehydrogenation Catalysts, *ACS Catal.*, 2016, **6**(4), 2257–2264; (*b*) N. Kaylor and R. J. Davis, Propane dehydrogenation over supported Pt–Sn nanoparticles, *J. Catal.*, 2018, **367**, 181–193.

6 J. J. H. B. Sattler, J. Ruiz-Martinez, E. Santillan-Jimenez and B. M. Weckhuysen, Catalytic Dehydrogenation of Light Alkanes on Metals and Metal Oxides, *Chem. Rev.*, 2014, **114**(20), 10613–10653.

7 (*a*) V. J. Cybulskis, B. C. Bukowski, H.-T. Tseng, J. R. Gallagher, Z. Wu, E. Wegener, A. J. Kropf, B. Ravel, F. H. Ribeiro, J. Greeley and J. T. Miller, Zinc Promotion of Platinum for Catalytic Light Alkane Dehydrogenation: Insights into Geometric and Electronic Effects, *ACS Catal.*, 2017, **7**(6), 4173–4181; (*b*) E. C. Wegener, Z. Wu, H.-T. Tseng, J. R. Gallagher, Y. Ren, R. E. Diaz, F. H. Ribeiro and J. T. Miller, Structure and reactivity of Pt–In intermetallic alloy nanoparticles: Highly selective catalysts for ethane dehydrogenation, *Catal. Today*, 2018, **299**, 146–153; (*c*) S. C. Purdy, P. Ghanekar, G. Mitchell, A. J. Kropf, D. Y. Zemlyanov, Y. Ren, F. Ribeiro, W. N. Delgass, J. Greeley and J. T. Miller, Origin of Electronic Modification of Platinum in a Pt_3V Alloy and Its Consequences for Propane Dehydrogenation Catalysis, *ACS Appl. Energy Mater.*, 2020, **3**(2), 1410–1422.

8 C. Ye, M. Peng, Y. Wang, N. Zhang, D. Wang, M. Jiao and J. T. Miller, Surface Hexagonal Pt_1Sn_1 Intermetallic on Pt Nanoparticles for Selective Propane Dehydrogenation, *ACS Appl. Mater. Interfaces*, 2020, **12**(23), 25903–25909.

9 (*a*) Z. Qi, C. Xiao, C. Liu, T. W. Goh, L. Zhou, R. Maligal-Ganesh, Y. Pei, X. Li, L. A. Curtiss and W. Huang, Sub-4 nm PtZn Intermetallic Nanoparticles for Enhanced Mass and Specific Activities in Catalytic Electrooxidation Reaction, *J. Am. Chem. Soc.*, 2017, **139**(13), 4762–4768; (*b*) Q. Chen, J. Zhang, Y. Jia, Z. Jiang, Z. Xie and L. Zheng, Wet chemical synthesis of intermetallic Pt_3Zn nanocrystals via weak reduction reaction together with UPD process and their excellent electrocatalytic performances, *Nanoscale*, 2014, **6**(12), 7019–7024; (*c*) Y. Kang, J. B. Pyo, X. Ye, T. R. Gordon and C. B. Murray, Synthesis, Shape Control, and Methanol Electro-oxidation Properties of Pt–Zn Alloy and Pt_3Zn Intermetallic Nanocrystals, *ACS Nano*, 2012, **6**(6), 5642–5647; (*d*) A. Miura, H. Wang, B. M. Leonard, H. D. Abruña and F. J. DiSalvo, Synthesis of Intermetallic PtZn Nanoparticles by Reaction of Pt Nanoparticles with Zn Vapor and Their Application as Fuel Cell Catalysts, *Chem. Mater.*, 2009, **21**(13), 2661–2667.

10 S. Iihama, S. Furukawa and T. Komatsu, Efficient Catalytic System for Chemoselective Hydrogenation of Halonitrobenzene to Haloaniline Using PtZn Intermetallic Compound, *ACS Catal.*, 2016, **6**(2), 742–746.

11 J. Camacho-Bunquin, M. S. Ferrandon, H. Sohn, A. J. Kropf, C. Yang, J. Wen, R. A. Hackler, C. Liu, G. Celik, C. L. Marshall, P. C. Stair and M. Delferro, Atomically Precise Strategy to a PtZn Alloy Nanocluster Catalyst for the Deep Dehydrogenation of n-Butane to 1,3-Butadiene, *ACS Catal.*, 2018, **8**(11), 10058–10063.

12 (*a*) M. W. Schreiber, C. P. Plaisance, M. Baumgartl, K. Reuter, A. Jentys, R. Bermejo-Deval and J. A. Lercher, Lewis-Bronsted Acid Pairs in Ga/H-ZSM-5 To Catalyze Dehydrogenation of Light Alkanes, *J. Am. Chem. Soc.*, 2018, **140**(14), 4849–4859; (*b*) J. J. H. S. Ruiz-Martinez, J. Santillan-Jimenez and B. M. Weckhuysen, Catalytic

Dehydrogenation of Light Alkanes on Metals and Metal Oxides, *Chem. Rev.*, 2014, **114**, 10613–10653.

13 (*a*) L. Rochlitz, K. Searles, J. Alfke, D. Zemlyanov, O. V. Safonova and C. Copéret, Silica-supported, narrowly distributed, subnanometric Pt–Zn particles from single sites with high propane dehydrogenation performance, *Chem. Sci.*, 2020, **11**(6), 1549–1555; (*b*) P. Ingale, K. Knemeyer, P. Preikschas, M. Ye, M. Geske, R. Naumann d'Alnoncourt, A. Thomas and F. Rosowski, Design of PtZn nanoalloy catalysts for propane dehydrogenation through interface tailoring via atomic layer deposition, *Catal. Sci. Technol.*, 2021, **11**(2), 484–493.

14 (*a*) S. M. George, Atomic Layer Deposition: An Overview, *Chem. Rev.*, 2010, **110**(1), 111–131; (*b*) B. S. Lim, A. Rahtu and R. G. Gordon, Atomic Layer Deposition of Transition Metals, *Nat. Mater.*, 2003, **2**(11), 749–754.

15 J. A. Libera, J. W. Elam and M. J. Pellin, Conformal ZnO coatings on high surface area silica gel using atomic layer deposition, *Thin Solid Films*, 2008, **516**(18), 6158–6166.

16 Z. Moser, The Pt–Zn (Platinum-Zinc) system, *J. Phase Equilib.*, 1991, **12**(4), 439–443.

17 J. W. Elam and S. M. George, Growth of ZnO/Al_2O_3 Alloy Films using Atomic Layer Deposition Techniques, *Chem. Mater.*, 2003, **15**(4), 1020–1028.

18 J. D. Ferguson, A. W. Weimer and S. M. George, Surface chemistry and infrared absorbance changes during ZnO atomic layer deposition on ZrO_2 and $BaTiO_3$ particles, *J. Vac. Sci. Technol., A*, 2005, **23**(1), 118–125.

19 H. H. Sønsteby, A. Yanguas-Gil and J. W. Elam, Consistency and reproducibility in atomic layer deposition, *J. Vac. Sci. Technol., A*, 2020, **38**(2), 020804.

20 J. Zhu, X. Zheng, J. Wang, Z. X. Wu, L. L. Han, R. Q. Lin, H. L. L. Xin and D. L. Wang, Structurally ordered Pt–Zn/C series nanoparticles as efficient anode catalysts for formic acid electrooxidation, *J. Mater. Chem. A*, 2015, **3**(44), 22129–22135.

21 Y. Lei, J. Jelic, L. C. Nitsche, R. Meyer and J. T. Miller, Effect of Particle Size and Adsorbates on the L_3, L_2 and L_1 X-ray Absorption Near Edge Structure of Supported Pt Nanoparticles, *Top. Catal.*, 2011, **54**, 334–348.

22 J. M. Ramallo-López, F. G. Requejo, A. F. Craievich, J. Wei, M. Avalos-Borja and E. Iglesia, Complementary methods for cluster size distribution measurements: supported platinum nanoclusters in methane reforming catalysts, *J. Mol. Catal. A: Chem.*, 2005, **228**(1), 299–307.

23 T. J. Penfold, J. Szlachetko, F. G. Santomauro, A. Britz, W. Gawelda, G. Doumy, A. M. March, S. H. Southworth, J. Rittmann, R. Abela, M. Chergui and C. J. Milne, Revealing hole trapping in zinc oxide nanoparticles by time-resolved X-ray spectroscopy, *Nat. Commun.*, 2018, **9**(1), 478.

24 (*a*) Y. Lei, S. Lee, K.-B. Low, C. L. Marshall and J. W. Elam, Combining Electronic and Geometric Effects of ZnO-Promoted Pt Nanocatalysts for Aqueous Phase Reforming of 1-Propanol, *ACS Catal.*, 2016, **6**(6), 3457–3460; (*b*) K. Fottinger, J. A. Van Bokhoven, M. Nachtegaal and G. Rupprechter, Dynamic Structure of a Working Methanol Steam Reforming Catalyst: *In Situ* Quick-EXAFS on Pd/ZnO Nanoparticles, *J. Phys. Chem. Lett.*, 2011, **2**, 428–433.

25 F. Behafarid, S. Pandey, R. E. Diaz, E. A. Stach and B. R. Cuenya, An *in situ* transmission electron microscopy study of sintering and redispersion phenomena over size-selected metal nanoparticles: environmental effects, *Phys. Chem. Chem. Phys.*, 2014, **16**(34), 18176–18184.